Plasma Research Express

PAPER

Genesis of non-uniformity of plasma fluxes over emissive wall in low-temperature plasmas

To cite this article: I V Schweigert *et al* 2019 *Plasma Res. Express* **1** 045007

Plasma Research Express

PAPER

RECEIVED
11 July 2019

REVISED
20 November 2019

ACCEPTED FOR PUBLICATION
25 November 2019

PUBLISHED
3 December 2019

Genesis of non-uniformity of plasma fluxes over emissive wall in low-temperature plasmas

I V Schweigert[1], M L R Walker[2] and M Keidar[1]

[1] George Washington University, Washington D.C. 20052, United States of America
[2] Georgia Institute of Technology, Atlanta, Georgia 30332, United States of America

E-mail: ivschweigert@email.gwu.edu

Keywords: non-uniform plasma flux, secondary electron emission, grooved surface, segmented surface, oblique magnetic field

Abstract

Origins of spatial modulation of stationary electron and ion currents to the wall in discharge plasma with/without magnetic field at low gas pressure are studied in the experiments and 2D PIC MCC simulations. It is shown that a non-uniformity of ion and electron fluxes to the wall is induced by (a) a non-planar topology on the emissive wall, (b) a difference in the secondary electron emission yields of materials in segmented wall or (c) an inclination of the external magnetic field. The transition in the sheath structure over the grooved emissive surface from a developed sheath to a collapsed one caused by the increase of electron energy enlarges the alteration of the ion and electron currents over the grooved or segmented surfaces. The experimental study of the plasma-emissive wall sheath transition was carried out with hexagonal boron nitride wall samples grooved with the characteristic size of 1 mm and 5 mm, which is about of the Debye length. In kinetic simulations, this phenomenon is analyzed in terms of the electron and ion energy distribution functions. An external oblique magnetic field applied to the dc discharge is found to redistribute the plasma and the periodical structure with the spikes of electron and ion densities forms This phenomena causes the non-uniform spatial distribution of electron and ion currents to the wall. The spikes in electron and ion densities became more pronounced with an increase of magnetic field incidence angle.

1. Introduction

A spatial non-uniformity of electron and ion fluxes on the treated surfaces in plasma devices can be provoked by various factors, for example, a non-planar surface topology, difference in the electron emission yield of materials in the segmented surface or presence of an oblique external magnetic field. In these cases, feedback between plasma and surface structure (through the non-planar surface sheath) can lead to an essential modification of the surface during device operation and drastic change of all plasma characteristics.

For example, in Hall effect thrusters, plasma—wall interaction was found to play a key role in the thruster operation and performance [1–6]. Radially-symmetric surface modulations, at a larger characteristic length scale than the plasma sheath thickness were observed in [1, 3]. In [7], sub-micron erosion patterns founded in a hexagonal boron nitride—amorphous silica Hall effect thruster's wall in [7], material in a krypton plasma. Using different metallographically-polished hBN surface finishes, the influence of roughness on plasma sheath potential was observed in [8].

The secondary electron emission (SEE) yield from the wall can be different for smooth or rough surfaces, that affects the plasma sheath structure. Effects of surface features smaller-than-Debye length scales on SEE were previously found to be consistent with a trapping of the secondary electrons near the wall surface [9].

The interaction of low temperature plasma with a planar emissive wall has been studied quite intensively since the original work of Hobbs and Wesson [10]. Materials with enhanced secondary electron yield used for manufacturing in discharge chambers change the classical concept of the Debye sheath, screening plasma from

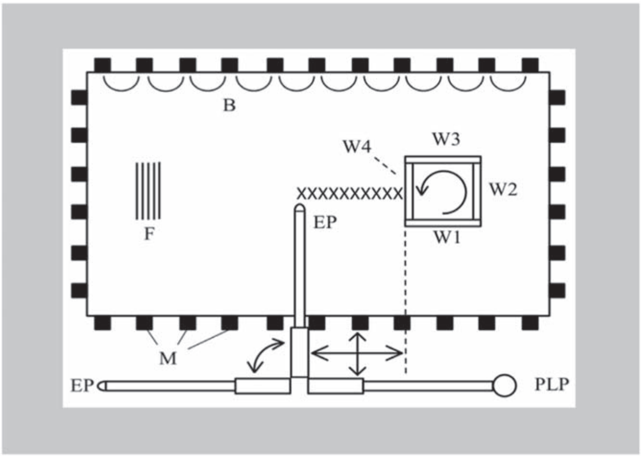

Figure 1. Sketch of plasma cell, F = filaments, M = magnets, B = magnetic field, PLP = planar Langmuir probe, EP = emissive probe, W = wall material sample, X = data measurement location. Emissive probe orientation rotated 90 degrees in the figure to show hairpin tip geometry.

the surface [11–16]. Nevertheless for the complex wall topology the mechanism of formation of plasma-material sheath is not clear yet.

Another reason of the spatial non-uniformity of electron and ion current is an occurrence of the external magnetic field. Applying the oblique magnetic field to the plasma causes the formation of periodic plasma structure [17]. For the first time, the magnetic striation due to the instability was theoretically analyzed in [18, 19]. The stratification of plasma causes the modulation of charged particle flux over the planar wall.

The application of oblique magnetic field with respect to the channel walls in the Hall effect thruster for better controlling the characteristics of the devices was discussed in [20, 21]. Nevertheless, discharge plasma parameters can essentially vary with with an increase of the inclination of the magnetic field. In the laboratory experiment with this type of plasma [22], a several stationary, magnetized, two-dimensional weak double-layers were registered. A weak double-layer is a nonlinear electrostatic structure in plasmas, consisting of two sheets of positive and negative charges, with a characteristic electric potential jump, providing local electric field. In early 1980s the effect of oblique magnetic field on the plasma was studied by Borovsky, Joyce [23]. In PIC simulations it was shown that a weak magnetization results in the double-layer electric-field alignment of particles accelerated by these potential structures. Recently, most of the studies have addressed strong or ion acoustic double-layer in magnetized plasmas [24–28], while the mechanism of weak double-layer formation in oblique magnetic field is not considered.

In this paper, the spatial variations of electron and ion fluxes over the emissive wall caused by the Debye length grooves, segmented structure of the surface and inclined magnetic field are studied in the experiment and kinetic simulations.

The paper is organized as follows. Experimental setup and diagnostics are described in section 2. Theoretical model and calculation details are given in section 3. The transition in the sheath structure over the emissive planar surface is discussed in section 4. In section 5, the experimental and simulation results on the sheath transition over the grooved sample is presented. A non-uniformity of ion flux bombarding the grooved emissive surface is described in section 6. In section 7, an alternating of ion flux over the segmented planar surface made from materials with different secondary electron yields is analyzed. An effect of inclined magnetic field on the spatial distribution electron and ion fluxes in the discharge is discussed in section 8. The conclusions are given in section 9.

2. Experimental setup and diagnostics

A multidipole plasma device shown in figure 1 is used for the experimental study of plasma-emissive wall interaction. The cylindrical plasma chamber has a radius of 30.5 cm and a height of 91 cm. The chamber is grounded and has a low secondary electron emission yield. The direct current discharge glows at P = 0.1 mTorr in argon. The electrons emitted from a tungsten filament (F in figure 1) are accelerated crossing the cathode sheath in the direction of the wall material sample (W in figure 1). These electrons form almost a monoenergetic beam with the energy corresponding to the cathode voltage *U*, which varies from −60 V to −350 V. This beam electron current *j* ranges ranges from 10 mA to 40 mA. The permanent magnet dipoles around the plasma chamber wall produce a cusp magnetic field (B in figure 1). This magnetic field confines the plasma, but decays quickly away from the wall of the chamber, so the main plasma volume is not magnetized. This device is similar to the original design by Limpaecher and Mackenzie [29] and also used in the experiments of Hershkowitz [30]. Different from previous work, we operate the device at a low discharge current of (10–40) mA to allow the energetic electrons from the cathode to become a significant population in the plasma. This increases the average electron energy of the plasma and elicits high SEE yields from the wall materials.

The target sample made from Al_2O_3 or BN (W in figure 1) has an enhanced secondary electron emission (SEE) coefficient and is placed 40 cm apart from the cathode. The measurements of the sheath structure are carried out near this dielectric emissive plate, which is electrically isolated. Typical plasma density used was approximately $10^7 cm^{-3}$ and with 1%–10% of the energetic electrons population.

The plasma cell is installed in a larger vacuum chamber which has a pressure of 10^{-8} Torr. During operation, the experimental pressure of $P = 0.1$ mTorr is achieved with 500 sccm of argon flow into the chamber using an MKS 1179A01352CS1BV mass flow controller.

The sheath potential distribution over the wall material samples was measured using an emissive probe constructed of telescoping alumina tubing and a hairpin 0.127 mm diameter thoriated tungsten filament tip. The emissive probe is biased with a Keithley 2410 Sourcemeter. Bulk plasma parameters are measured using a planar Langmuir probe positioned in the center of the plasma device. Before data collection the probe is cleaned by ion bombardment at −500 V bias for a period of 15 min. The probe was re-cleaned at −500 V for 30 s after the collection of each trace. The probe characteristics were corrected for singly-charged argon ion- and electron-induced SEE using data for tungsten from [31]. The planar probe data was found to agree well to the equation for the probe current from the primary electrons from [32], and a bi-Maxwellian plasma by the analysis from [33], correcting all for the secondary electron emission of the tungsten probe tip using the data of Hagstrum [34].

3. Theoretical model and calculation details

In our theoretical model, the discharge plasma in electromagnetic fields at low gas pressure is described with solving Boltzmann equations (two dimensional in space and three dimensional in velocity space) for the distribution functions for electrons $f_e(\vec{r}, \vec{v})$ and ions $f_i(\vec{r}, \vec{v})$

$$\frac{\partial f_e}{\partial t} + \vec{v}_e \frac{\partial f_e}{\partial \vec{r}} - \frac{e(\vec{E} + \vec{v}_e \vec{B})}{m} \frac{\partial f_e}{\partial \vec{v}_e} = J_e, \quad n_e = \int f_e d\vec{v}_e, \tag{1}$$

$$\frac{\partial f_i}{\partial t} + \vec{v}_i \frac{\partial f_i}{\partial \vec{r}} + \frac{e\vec{E}}{M} \frac{\partial f_i}{\partial \vec{v}_i} = J_i, \quad n_i = \int f_i d\vec{v}_i, \tag{2}$$

where v_e, v_i, n_e, n_i, m, M are the electron and ion velocities, densities and masses, respectively. J_e and J_i are the collisional integrals for electrons and ions. No magnetic field due to currents in the plasma is considered.

Poisson's equation describes the electric potential and electric field distributions

$$\triangle\phi = \frac{e(n_e - n_i)}{\epsilon_0}, \quad \vec{E} = -\frac{\partial \phi}{\partial \vec{r}}. \tag{3}$$

The boundary conditions for Poisson's equation are the voltage $U = U_0$ on the cathode and $U = 0$ on the grounded wall of the chamber. Since the wall sample is under the floating potential in plasma, the total current on it is zero

$$j_{be} + j_{pe} + j_i + j_{es} + j_{esr} = 0, \tag{4}$$

where j_{be}, j_{pe} are the currents of energetic beam electrons and low energy electrons from plasma, respectively, j_i is the ion current, j_{es} and j_{esr} are the currents of secondary electrons emitted from the sample surface and returning back to the surface, respectively.

The equations (1)–(3) are solved self-consistently with the 2D3V Particle-in-Cell Monte Carlo collisions method (2D3V PIC MCC) [35, 36]. In PIC MCC simulations, to find the floating potential of the sample plate we a) calculate electron and ion fluxes to the sample plate on every electron time step and if the total flux is not zero within 5% of statistical error, then b) the potential of the sample surface is tuned with a small voltage step of 0.1 V to improve the zero-current balance. As a result, the potential and the field distributions in plasma and on the sample plate surface reach a steady-state which depends on the energy of the electron beam. This floating potential of the sample surface is the boundary condition for the electric potential.

The kinetics of electrons in argon includes elastic scattering of electrons on background atoms, excitation of metastable states, and ionization. The cross sections of electron scattering are taken from [37, 38]. For Ar^+ ions, the elastic collision on background atoms with isotropic scattering and resonant charge exchange collision, or backward elastic scattering are taken into account.

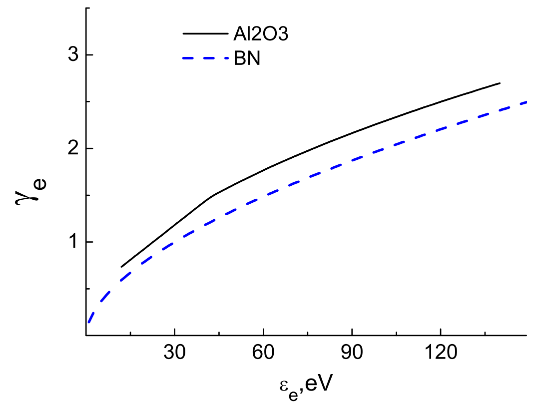

Figure 2. Secondary electron emission coefficient as a function of the electron energy for Al_2O_3 and *BN* materials.

In simulations as well as the experiment the wall sample is made from Al_2O_3 or *BN*. These materials have enhanced SEE coefficient γ_e shown in figure 2, which increases with the energy of an impinging electron [39].

The electron emission is simulated with the energy distribution functions of electrons approaching the sample wall. In simulations, we assume that no secondary electron emission for electrons with the energy ε_e less than 10 eV. If $\varepsilon_e \geqslant 10$ eV and $\gamma_e(\varepsilon_e) < 1$, a random number (RN) is computed from a uniformly distributed random numbers in the interval [0,1]. Then if RN $< \gamma_e(\varepsilon_e)$, a secondary electron with the weight of an incident pseudo electron (w_e) is emitted from the surface. The term 'weight' corresponds to the number of electrons in a pseudo electron, which is a group with the same velocity and coordinate and varies with the plasma density, $w_e = (2 \div 4) \times 10^4$. If $\gamma_e(\varepsilon_e) > 1$, a secondary electron with the weight $w_e \times \gamma_e(\varepsilon_e)$ is emitted. The emitted electrons have a half-Maxwellian distribution with $T_e = 0.1$ eV.

This 2D3V PIC MCC method is based on the sampling of EEDF and IEDF with pseudo particles. In the limit of small time steps and a large number of pseudo particles, the PIC-MCC model was shown in [40] converges to a solution of the Boltzmann equation. The simulations are performed with 2D3V PlasmaNov code developed by Schweigert VA and Schweigert IV

The simulation grid step is less compared to the Debye length. The time step is $\Delta t = (0.5 - 5) \times 10^{-12} s$, and it is much less than the Courant number ($\Delta z/v_e \simeq (10^{-11} - 10^{-10}) s$) for different considered cases. In our case, the plasma frequency $\omega_e \simeq 10^9 s^{-1}$ and the electron scattering frequency $\nu_e \simeq 10^7 s^{-1}$ gives less restriction for the time step. The number of pseudo particles for every type of species varies within a range of $(2 \div 4) \times 10^6$ depending on the plasma conditions.

4. Transition in sheath structure over emissive planar sample

In our experiment, the rearrangement of the sheath between plasma and the emissive sample was observed to be driven by an increase of applied voltage. Let us first consider the sheath transition near the planar emissive sample, which is the control sample for the study of the grooved surface sheath transition. The parameters of discharge plasma for different applied voltages were calculated solving equations (1)–(4)for the conditions of the experiment. The model cylindrical chamber has a radius of 20 cm and a height of 50 cm. The biased cathode (a filament in the experiment) is at z = 5.6 cm, and Al_2O_3 or *BN* wall sample is at z = 42 cm. The cathode and wall samples have a shape of a disk with a radius of 5 cm. The SEE yield from the sample is set with the SEE coefficient shown in figure 2 and the energy distribution function of electrons bombarding the sample surface.

The rate of electron thermoemission from the cathode is varied in simulations to provide a value of discharge current measured in the experiment, $j = (10–40)$ mA. The calculation domain and an example of the spatial distribution of the electron density n_e is shown in figure 3 for $U = -70$ V and $j = 30$ mA.

In simulations, the electrons emitted from the cathode gain the large kinetic energy crossing the cathode sheath. These electrons have a large longitudinal component of velocity, $v_z \gg v_x, v_y$ and form a beam directed toward the emissive wall sample. The beam electrons provide the ionization rate $\nu_i \approx 10^{13} cm^{-3}s^{-1}$ in the discharge volume for our plasma parameters. Another group of electrons (so called plasma electrons) has a lower mean energy and is accumulated in the volume. The fraction of beam electrons is less than 2%.

In simulations, as well as in the experiments [16], the plasma density varies from $10^7 cm^{-3}$ to 5×10^8 cm^{-3} for the different *U* and *j*. The quasineutral plasma occupies the center part of the chamber volume. The Debye sheaths separate plasma from non-emissive walls of the chamber and is indicated in figure 3 with almost zero n_e zones.

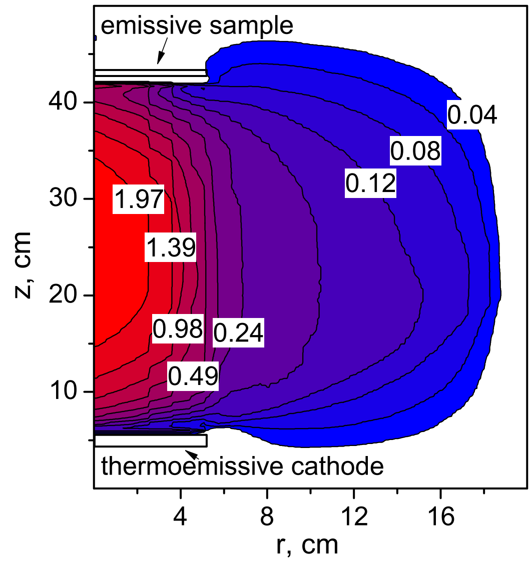

Figure 3. Electron density normalized with $10^8 cm^{-3}$ for thermo-emission current $j = 30$ mA and the applied voltage U = −70 V. The axis of symmetry of the cylindrical chamber is at r = 0.

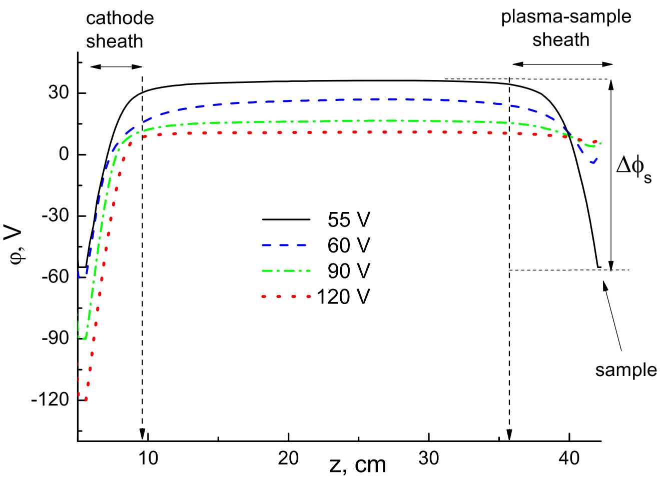

Figure 4. Potential profiles over the axis of symmetry for $U = -55$ V, −60 V, −90 V and −120 V and for thermo-emission current $j = 20$ mA and Al_2O_3 sample.

4.1. Three types of sheaths near the emissive wall sample

The electrons emitted from the cathode form almost monoenergetic beam since they cross the cathode sheath practically without collisions. With increasing voltage U, the energy of beam electrons rises. Approaching the wall sample the electrons with larger energy provide more pronounced secondary electron emission, that causes the plasma-sample sheath rearrangement. In figure 4, a change of the potential profile with the voltage increase is shown for $j = 20$ mA. The potential drop near the wall sample relatively the quasineutral plasma is shown with $\Delta\phi_s$. Vertical arrows show the place of calculation of the electron energy distribution function that will be discussed below. The potential drop over the cathode sheath increases with the negative cathode bias, whereas the plasma potential slightly decreases. Both in the experiment and simulation a non-monotonic decrease of the sheath over the wall sample was observed with a rise of the beam electron energy. At some critical U, the plasma-sample sheath collapses. The non-monotonic behavior of $\Delta\phi_s$ is associated with a change of the currents balance to the wall sample. The measured and calculated potential distribution near the wall sample are shown in figure 5 for the negative bias ranging from −60 V to −120 V. The potential profiles are given relative to the plasma potential. The computed and measured $\Delta\phi_s$ coincide within 10% error.

A virtual cathode appears due to an excess of slow secondary electrons emitted from the sample. It shows up as a dip on the potential profile near the wall sample in simulation (see figure 5(a)). No virtual cathode was observed in the experiments, which may be due to insufficient probe resolution near the wall.

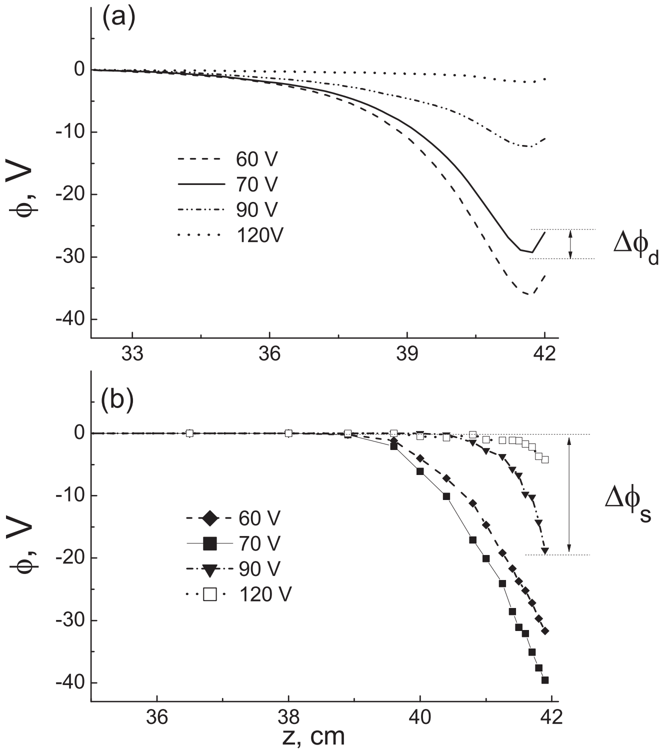

Figure 5. Calculated (a) and measured (b) potential profile (shown relative to the bulk plasma potential) near the emissive Al_2O_3 sample for U = −60 V, −70 V, −90 V and −120 V at j = 10 mA. $\Delta\phi_s$ is the sheath sample potential drop and $\Delta\phi_d$ is the depth of the virtual cathode.

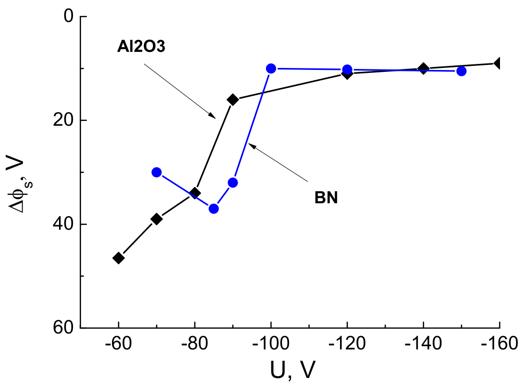

Figure 6. Calculated potential drop near the emissive wall samples made from Al_2O_3 and *BN* for different voltage and j = 10 mA.

In figure 6, the potential drop over the plasma-sample sheath is shown for wall samples made from Al_2O_3 and *BN* for the discharge current j = 10 mA. The *BN* material has a lower SEE yield, and the transition between developed and collapsed types of sheath takes place at a higher voltage.

The potential drop on the plasma-sample sheath $\Delta\phi_s$ and the depth of the virtual cathode dip $\Delta\phi_d$ are shown in figure 7 for higher discharge currents j = 20 mA and 40 mA. It is seen that three types of sheathes between plasma and emissive sample can be distinguished and the transition between them is driven by changing the cathode negative bias *U*.

The Debye sheath is shown in figure 7(a), a square D, occurs at lower voltage $|U| < 60$ V, when the secondary electron emission from the sample is negligible. For this type of sheath $\Delta\phi_s$ is about the cathode sheath potential drop (see figure 4) and only beam electrons approach the emissive sample.

Developed sheath. With increasing *U*, the transition from the Debye sheath (D) to the developed sheath with beam electron emission (BEE) takes place at $|U| = 60$ V. This transition is induced by switching on the secondary electron emission and accompanied by a considerable rise of the electron current from the plasma to the sample. After the transition between D sheath and BEE one, the electron current to the sample rises by two

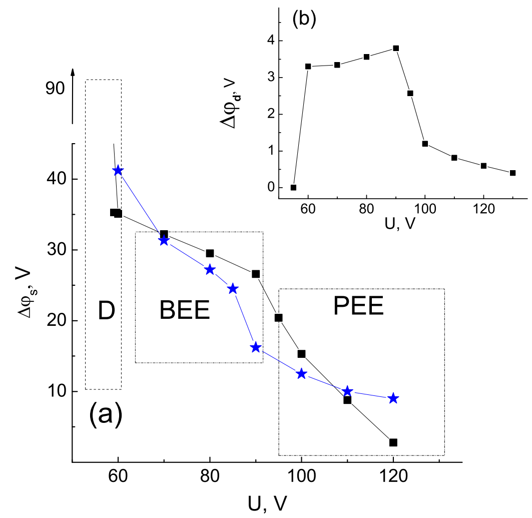

Figure 7. Potential drop over the sheath near the sample $\Delta\phi_s$ relative to the plasma potential for $j = 20$ mA (squares) and $j = 40$ mA (stars) (a) and the virtual cathode dip depth $\Delta\phi_d$ relative to the sample surface potential for $j = 20$ mA (b). Debye sheath (D), electron beam emission sheath (BEE) and plasma electron emission sheath (PEE). Figure 6 in [16].

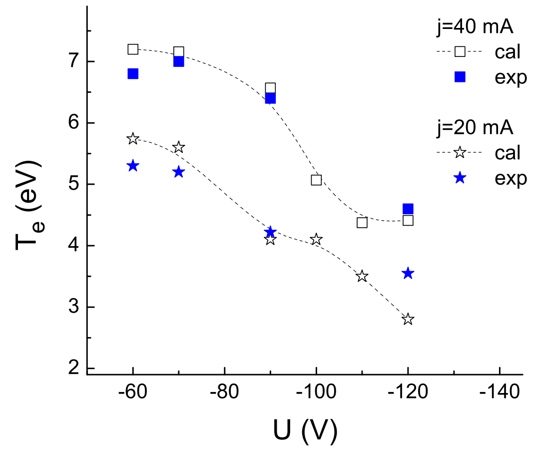

Figure 8. Mean electron temperature of plasma electrons in the center of the discharge as a function of negative bias on the cathode for j = 20 mA (stars) and 40 mA (squares). The open symbols are from simulations, and closed symbols are from the experiment. Figure 8 in [16].

orders of magnitude. Now the ion current is negligible compared to the electron one. The contributions of the beam electron current and the secondary electron current determine the floating sample potential, $j_{be} = j_{es} - j_{esr}$, where j_{esr} is the secondary electrons, scattering back to the sample by the virtual cathode.

Since the potential drop over the sample sheath decreases after the transition, the beam electrons approach the sample with the energy larger than 40 eV. In this case, the secondary electron emission yield is $\gamma_e > 1$, and the virtual cathode appears after the transition. With further increase of the electron beam energy (with increasing U) the potential dip of the virtual cathode becomes larger, returning more secondaries back to the surface. This increase of the potential dip helps the BEE sheath to retain over some range of voltage.

In simulations, the mean temperature of emitted electrons was $T_e = 0.1$ eV. We have checked the influence of the energy of secondary electrons ε_s and their initial positions δz from the emissive plate on the virtual cathode parameters. The ε_s was varied from 0.03 eV to 0.3 eV for different runs and δz ranges from 0.01 cm to 0.05 cm with a random distribution. We always observed the virtual cathode (a dip of the potential) and the depth and position of the virtual cathode changed within 30% for this range of parameters.

The measured and calculated mean temperature of the plasma electrons T_e in the quasineutral plasma as a function of U is shown in figure 8. In the BEE regime, the potential drop over the sample sheath is essentially larger than the mean energy of plasma electrons, $\Delta\phi_s/T_e \approx 4 \div 5$.

Collapsed sheath with plasma electron emission (PEE). The second transition is smooth and happens at U $\approx$ 90 V for the discharge current ranged from 10 mA to 40 mA. It is indicated in figure 7 by a faster decrease

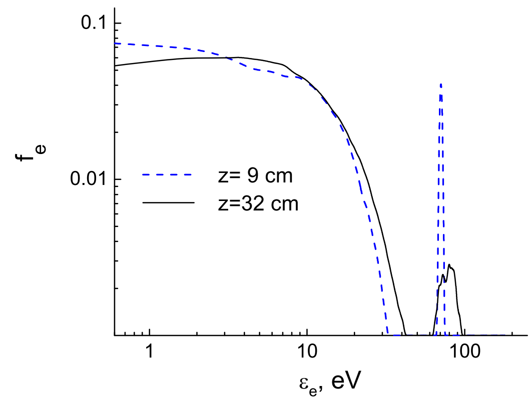

Figure 9. Electron energy distribution at z = 9 cm, r = 0 (dashed line), and at z = 32 cm, r = 0 (solid line) for $U = -70$ V, $j = 20$ mA. Figure 9 in [16].

Table 1. Negative bias (U), beam electron energy (ε_{be}), sample sheath potential drop ($\Delta\phi_s$), mean temperature of plasma electrons (T_e), virtual cathode potential dip ($\Delta\phi_d$) for $j = 20$ mA.

U	70 V	95 V	120 V
ε_{be}	84 eV	115 eV	130 eV
$\Delta\phi_s$	35.1 V	20.4 V	2.9 V
T_e	5.7 eV	4.2 eV	2.8 eV
$\Delta\phi_d$	3.3 eV	2.56 eV	0.57 eV

of the sample sheath potential drop and shrinking the virtual cathode. The mean temperature of the plasma electrons T_e also decreases at the point of the transition. In this new regime, the cold plasma electrons start to contribute to the zero-current balance on the sample surface. Now the currents of the cold plasma electrons j_{pe}, beam electrons j_{be} and secondary electrons, $j_{be} + j_{pe} = j_{se} + j_{ser}$ set the sample floating potential ϕ_s. The term j_{ser} becomes comparably small, because the virtual cathode practically disappeared (see figure 5(b)). Since the density of the plasma electrons is much larger compared to the beam electron one, a small diminishing the potential drop over the sample sheath, $\Delta\phi_s$, leads to a considerable increase of the plasma electron current to the sample. With increasing U the $\Delta\phi_s$ tends to $1T_e$.

The sheath over the emissive sample is quasi stationary in BEE and PEE regimes. This is related to the accumulation of secondary electrons near the surface. The sheath oscillation frequency of about 25 kHz is set by the secondary electrons yield and the ion velocity.

4.2. Electron energy distribution function

The electrons emitted from negatively biased thermocathode compose a beam of the same radius as the cathode. This beam is directed to the emissive floating wall sample. The electron energy distribution functions shown in figure 9 was calculated on the axis of symmetry at cathode sheath-plasma boundary and in bulk plasma. The plasma parameters determining the shape of the EEDF for $j = 20$ mA are listed in the table. In figure 9, the EEDFs calculated at cathode sheath-plasma boundary (at x = 9 cm) and in bulk plasma (at z = 32 cm) exhibit peaks of the beam electrons with the energy of about 85 eV, which is equal to the cathode potential drop. The EEDF in bulk plasma has a peak with a wider distribution due to collisions with background atoms and oscillating nature of the sample sheath. The lower energy plasma electrons have a mean temperature of 6.5 eV. Since the potential drop over the sample sheath is 35 V for $U = -70$ V, the secondary electrons have sufficient energy for the ionization. These secondaries enrich the higher energy part of plasma electron spectrum.

To explain the transition between BEE and PEE sheath regimes in terms of EEDF, let us consider the spectrum of electrons arriving at the sample surface. In figure 10, the EEDF is shown for j = 20 mA and for different voltages. It is seen that already for $U = -70$ V, the energy of beam electrons approaching the sample surface is large enough ($\approx$50 eV) to provide $\gamma_e > 1$. The large potential drop screens the sample from the most plasma electrons. Therefore their fraction in the EEDF is small ($<$0.1%) compared to that of the beam electrons.

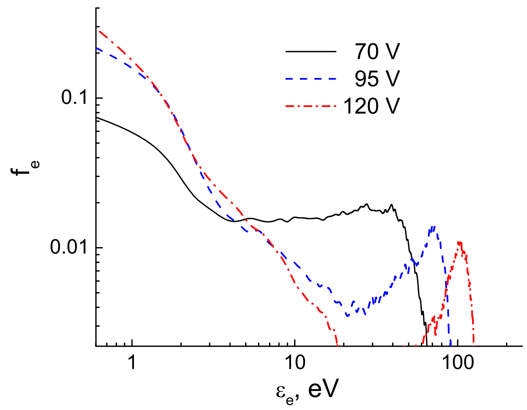

Figure 10. Energy distribution function for electrons, approaching the sample surface for U = −70 V (solid line), −95 V (dashed line) and −120 V (dash-dotted line) for j = 20 mA. Figure 10 in [16].

The energy distribution function of electrons arriving on the sample surface is not exactly a shifted EEDF at z = 32 cm, where a shift is the potential drop near the sample, $\Delta\phi_s$. Note that the sheath with a virtual cathode near the emissive surface always exhibits oscillatory behavior that allows the electrons with the energy smaller than the averaged sheath potential drop to cross the sheath.

With increasing voltage U, the shape of the EEDF changes qualitatively. A fraction of slow electrons from the plasma essentially increases as a result of the transition between the BEE and PEE regimes. At $U > 90$ V the beam electrons approaching the sample have the energy around 100 eV. They produce so many secondaries, that the sample sheath potential decreases, allowing the colder plasma electrons to reach the sample and support the zero-current balance. The virtual cathode becomes considerably smaller and less number of secondaries are repelling back to the sample. The formation of a virtual cathode near the emissive wall in a Maxwellian plasma was found previously in simulations [10] and observed in the experiment [41]. The electron current from the plasma to the sample is set both by plasma electrons and beam electrons, and the partial contribution of plasma electron current increases to 0.55 for $U = 120$ V.

In conclusion of this section, in kinetic (2D3V PIC MCC) simulations and the experiment we have studied the sheath rearrangement near the emissive floating wall sample with increasing applied voltage in a dc discharge plasma. The discharge operation in argon at P $= 10^{-4}$ Torr is maintained by the beam electrons emitted from negatively-biased thermo cathode. The planar emissive sample made from Al_2O_3 or *BN* materials placed some distance in front of the cathode is exposed to the beam electrons (with energy of 30 eV–120 eV) and plasma electrons (less than 8 eV). The secondary electron emission was calculated with accounting for the energy distribution functions of the electrons approaching the sample surface. Three types of sheaths have been distinguished near the floating emissive wall sample. The transition between them was driven by changing the cathode voltage from −55 V to −120 V, which sets the beam electron energy. *The Debye type of sheath* appears at low voltages at $|U| < 60$ V, when the secondary electron emission is negligible. With increasing U, the beam electrons bombard the sample with higher energy and the secondary electron emission switches on. It is accompanied by an abrupt decrease of the potential drop over the sample sheath and the electron current into the sample rises by two orders of magnitude. This is a transition between the Debye sheath and a new sheath of *beam electron emission (BEE)* type. In this regime, the ratio of the potential drop over the sample sheath to the temperature of plasma electrons is $\Delta\phi_s/T_e = 4 \div 5$. The floating potential of the sample is controlled by the beam electron current from plasma j_{be} and secondary electron current from the sample j_{es}, $j_{be} + j_{esr} = j_{es}$. The virtual cathode appears and helps to maintain the BEE regime within some voltage range from −60 V to −90 V. The virtual cathodes modification changes the back-scattering electron current j_{esr}. Further increase of cathode voltage initiates the smooth transition to *the plasma electron emission (PEE)* sheath regime. In this regime, the ratio $\Delta\phi_s/T_e$ tends to unity with increasing U and the current of plasma electrons to the sample considerably increase. The measured potential drop near the sample quantitatively agrees with the kinetic simulation results. Both measured and computed mean electron temperatures T_e in bulk plasma exhibit a decrease after the collapse of the sample sheath from 7 eV–8 eV to 4.7 eV–3.5 eV depending on the discharge current.

A variation of thermoemission current from negatively-biased cathode from 10 mA to 40 mA or a change of sample materials (Al_2O_3) do not affect the qualitative picture of sheath transitions.

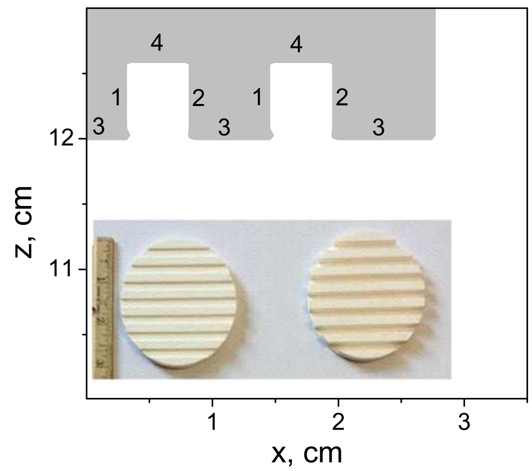

Figure 11. The geometry of grooves in simulations. 1, 2, 3, 4 show the different fragments of grooves for separate calculation of floating potential. Insert shows the photo of grooved samples in the experiment.

5. Transition in sheath structure over emissive wall sample with Debye-Scale Grooves

Let us consider the plasma sheath structure near the emissive wall sample with a complex topology. In the experiment, the sample with grooves on the surface was embedded in the plasma chamber shown in figure 1. As discussed in section 2, the electrons emitted from the thermoemissive cathode form almost a monoenergetic beam which provides the volume ionization and the secondary electron emission, bombarding the wall sample made from hBN material. This material has a large secondary electron emission yield which increases with the energy of incident electrons. It is also a commonly used ceramic wall material in Hall effect thrustes. In figure 11, the photo of samples is shown. They have a shape of disks with 7.6 cm in diameter and 0.64 cm in thickness. The 5 mm wide grooves are machined into the surface of the samples, which are spaced 10 mm apart with uniform depths of either 1 mm or 5 mm. A control disk with no grooves is also used for comparison. Prior to insertion into the plasma chamber, the disks were cleaned with acetone, deionized water then air dried. The hBN disks were mounted to a box holder made of stainless steel.

The sheath potential over the grooved material samples was measured using an emissive probe described in section 2.

5.1. Simulation: theoretical model for grooved wall-plasma interaction

In our PIC MCC simulations, to study features of the sheath structure near the grooved emissive sample in discharge plasma we use the model developed for the planar surface case and presented in section 3. The discharge plasma with the embedded grooved wall sample is described with the equations (1)–(4)in Cartesian coordinates and simulated for our experimental conditions with 2D3V PIC MCC method with PlasmaNov code (see for details [42]). The calculation domain is 13 cm over z-axis, 8 cm over x-axis and $\mathrm{x} = 0$ is the axis of symmetry. The cathode of 3.2 cm over x is placed 0.5 cm above the bottom of the chamber. For the Poisson equation the boundary conditions are $\phi = U$ at the cathode, $\phi = 0$ at $\mathrm{z} = 0$ and $\mathrm{z} = 13$ cm, the electric field $\mathrm{E}_x = 0$ at $\mathrm{x} = 8$ cm.

In figure 11, a part of calculation domain near the sample with grooves of 5 mm wide and 5 mm depth is shown. In simulations, the wall material sample has four identical trenches, but in figure 11, there are only two grooves shown, since $\mathrm{x} = 0$ is the axis of symmetry. Since the BN-disk is under the floating potential the total current on it $j_{total} = 0$. For the grooved sample the floating potential is calculated solving equation (4) separately for four different surface fragments shown in figure 11: for left (1) and right (2) sides of trenches, for front surface (3) and for trench bottom (4).

In simulations, we took a secondary electron emission coefficient γ_e in the form $\gamma_e = (\varepsilon_e/E)^{\alpha}$, where $E = 30$ and $\alpha = 0.67$. The secondary electron emission coefficient from [43], $\gamma_e = (\varepsilon_e/E)^{\alpha}$ with $E = 30$ and $\alpha = 0.57$. In the simulation a larger α is taken to obtain a better agreement with our experimental observations.

5.2. Features of sheath transition near the grooved wall sample. Experiment and simulations

In simulations and in the experiment, the volume ionization, as well as the secondary emission from the BN-wall sample are sustained by a beam of energetic electrons from the thermoemissive cathode. With changing applied

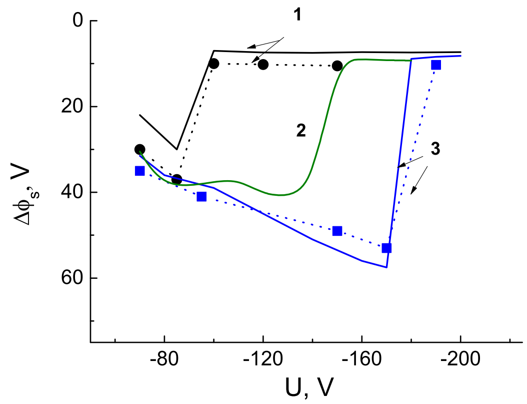

Figure 12. Potential drop near BN-wall sample as a function of applied voltage for planar (1) and grooved surfaces with a depth of 1 mm (2) and 5 mm (3). Experimental data (solid lines) and calculations (symbols). Figure 4 in [17].

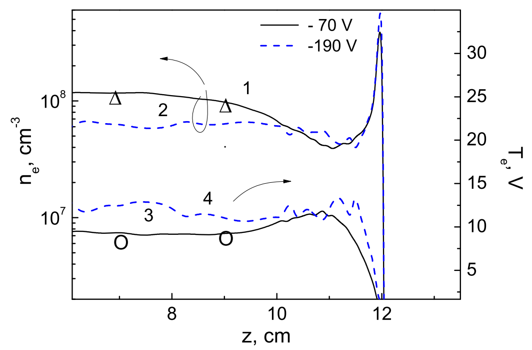

Figure 13. Electron density and temperature distributions over axis of symmetry for $U = -70$ V (1, 3) and -190 V (2, 4) for grooved surface. Symbols are the experimental data measured 3 cm and 5 cm apart from the grooved surface for $U = -70$ V. Figure 5 in [17].

voltage U from -70 V to -200 V, the energy of beam electrons rises linearly. It increases the SEE yield from the sample, since $\gamma_e(\varepsilon_e)$ is a growing function of the electron energy.

With increasing U, the sheath transition happens near BN-wall sample at some critical voltage U_{cr}. In figure 12, the potential drop $\Delta\phi_s$ between the bulk plasma and electrically isolated sample is shown for cases of grooved and planar surfaces. As seen in figure 12, both measured and calculated potential drops exhibit an abrupt transition from the developed to collapsed sheath types. During the transition the $\Delta\phi_s$ diminishes approximately in 3–5 times for both cases, but it happens at different voltages. For the planar sample, the transition takes places at $U_{cr} = -90$ V, for the 0.1 cm-grooves case $U_{cr} = -140$ V and for the 0.5 cm-grooves case $U_{cr} = -175$ V. Note that for grooves with $l = 0.5$ cm the critical voltage is approximately twice larger compared to the planar wall sample one. As seen in figure 12, a decrease of grooves characteristic size causes a lowering the critical voltage and in the limit of $l \ll \lambda_D$, the sheath development will not depend on surface topology. More complex processes take place for the case of larger grooves with $l \gg \lambda_D$ when sheaths form inside of the trenches, and the dynamics of electron heating essentially changes (see for example [44]).

The calculated and measured electron density n_e and the mean electron temperature T_e before and after the transition are shown in figure 13 for the grooved surface for $U = -70$ V and -190 V. In the experiment, the n_e and T_e were measured 3 cm and 5 cm apart from the emissive surface for U $= -70$ V. It is seen that after the transition the density of plasma decreases by a factor of two. The density of electrons increases near the surface due to the accumulation of emitted low energy secondary electrons. The calculated and measured electron temperature is averaged over all groups of electrons.

For all our experimental conditions $T_e = 8$–12 eV and the n_e is in a range of (5–10) $\times$ 10^7 cm^{-3} in a quasineutral plasma and (1–5) $\times$ 10^7 cm^{-3} within the sample sheath. The Debye length, $\lambda_D\,(\text{cm}) = 742 \times (T_e/n_e)^{0.5}$, ($T_e$ in eV and n_e in cm^{-3}), varies from 0.25 cm to 0.5 cm for our plasma parameters. The wall material samples in our study are grooved with a trench size $l \approx \lambda_D$ and the sheath could not form inside of the grooves.

The spatial distribution of n_e over the grooved sample after the transition (U $= -190$ V) and the potential profiles normal to the sample surface are shown in figure 14. The peaks of the density of low energy secondary

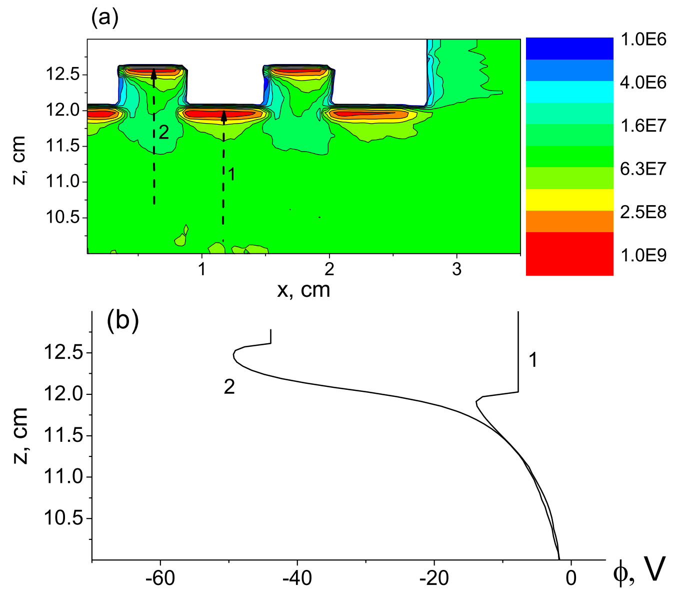

Figure 14. Spatial electron density distribution (a) and potential profiles (b) normal to the sample surface along dashed lines 1 and 2 for $U = -190$ V.

electrons and associated with them virtual cathodes arise near the emissive surface. The densities of energetic beam electrons and the low energy electrons in quasineutral plasma are $n_{be} = 0.26 \times 10^7$ cm^{-3} and $n_{pe} = 5.2 \times 10^7$ cm^{-3}, respectively. In figure 14(b), the potential distribution is given along the arrows (1) and (2) shown in figure 14(a). The virtual cathode looks like a dip in the potential profile near the emissive surface exposed to the energetic electrons.

Let us consider the mechanism responsible for a delay of the sheath transition near the grooved emissive surface compared to the planar control sample. For our experimental conditions, the sheath near the emissive surface forms depending on a contribution of secondary electrons even for the smaller applied voltage. The sheath is not a Debye-type, and the ion current to the surface is negligible. The zero-current condition to the surface under floating potential allows us roughly estimate a ratio of beam electron current j_{be} and the plasma electron one j_{pe} to the emissive sample

$$j_{pe} = j_{be} \times (\gamma_e(\varepsilon_e) - 1), \tag{5}$$

An increase of $\gamma_e(\varepsilon_e)$ with a rise of beam electron energy induces a decrease of a potential drop over the sample sheath to allow the j_{pe} to enlarge.

The question of why the critical voltage increases for the grooved surface case can be answered analyzing the electron energy distribution function (EEDF) and potential distribution over the surface.

In figure 15, EDFs of electrons approaching the planar and grooved samples on the axis of symmetry are shown for $U = -85$ V and -95 V, respectively. For both cases, the sheath potential drop $\Delta\phi_s \approx 40$ V (see insert in figure 15). Note that for the planar case the voltage $U = -85$ V is near the transition point, but for the grooved case, $U = -95$ V is essentially smaller than U_{cr}. For both cases the EEDFs have two groups of electrons, but for the grooved case, the population of a group of low energy plasma electrons is larger. Enrichment of this group is provided with a deflection of the flux of low energy electrons from the orifice of grooves to the front surface. This focusing effect is due to a non-monotonic potential distribution along the grooved surface. Note, that the flux of energetic beam electrons is weakly disturbed by the electric field E_x and it penetrates inside of grooves. Other words, the focusing the plasma electrons flux has a similar effect as a decrease of the sheath potential drop near the sample: it increases the flux of plasma electrons j_{pe} on the front surface without a collapse of the sample sheath. This explains the effect of increasing U_{cr} for the grooved surface.

The non-monotonic potential distribution near the wall sample with a strong gradient over x along the grooved surface was registered in our simulations and experiments. In figure 16, the measured and calculated spatial potential distribution near the grooved sample is shown for $U = -150$ V before the transition. In figure 16(a), the white arrows denote the trajectories of low energy electrons schematically. Figure 16(b) Shows the electric potential profile along the dashed line given in figure 16(a). The measurements of the electric potential shown in figure 16(c) were done with steps of 1 mm over the grooves surface and of 0.5 mm in the normal direction. The domain of measurement of 13 mm over x and 6 mm over z is 1 mm apart from the surface. The non-uniform electric potential distribution acts as a focusing lens on the low energy electrons flux

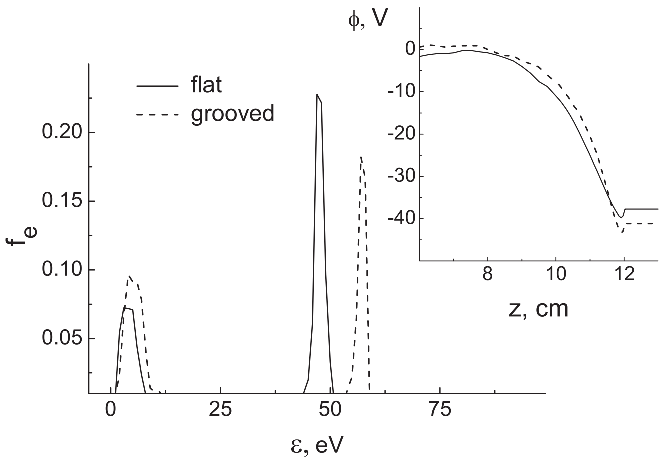

Figure 15. The electron energy distribution function for electrons approaching the front surface of planar (solid line) and grooved (dashed line) wall samples for $U = -85$ V and -95 V, respectively. In insert: potential profiles over z at $x = 0$ for planar (solid line) and grooved surfaces (dashed line). Figure 8 in [17].

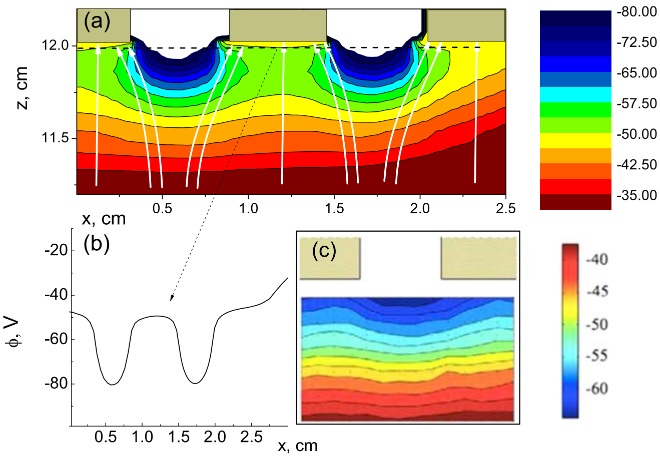

Figure 16. Electric potential distribution calculated (a), (b) and measured (c) for $U = -150$ V. The color map for (c) is from -35 V up to -70 V. White arrows show the electron trajectories schematically. (b) presents the potential profile along the dashed line shown in (a). Figure 9 in [17].

and redirects electrons to the front surface from the orifices of grooves. Note that these additional low energy electrons do not produce the secondary electrons from the surface. In another words, in the left hand of equation (5), the current j_{pe} increases approximately by a factor of two, therefore the critical voltage increases for the grooved case.

In conclusion of this section, the transition between different types of sheaths near the emissive surface with Debye length grooves in low-pressure plasma have been studied in the experiment and PIC MCC simulations. The ionization in the plasma volume and the secondary electron emission from the grooved wall sample are set by the beam electrons initiated from biased filaments. The hBN disks with machined grooves with 1 mm and 5 mm-depth on the surface were maintained in the plasma chamber to study the plasma interaction with the emissive surface with a complex topology. These grooves mimic different degrees of erosion on the wall in plasma. With increasing voltage, the measured and calculated potential distributions over the BN-wall sample exhibit transition between different types of sheaths. This transition has been found to take place at a higher applied voltage for the sample with larger grooves. For the case of grooves of 5 mm depth, the critical voltage is almost two times higher as compared to the planar control sample. An analysis of the energy distribution function of electrons arriving on the surface and the potential distribution allowed us to explain this phenomenon. In the case of grooved surface, a non-monotonic potential distribution along the grooves can deflect the flux of low energy electron from the orifice of grooves to the front surface, whereas the flux of beam electrons remains practically undisturbed. The electric field component parallel to the surface is not strong enough to affect the beam electron current.

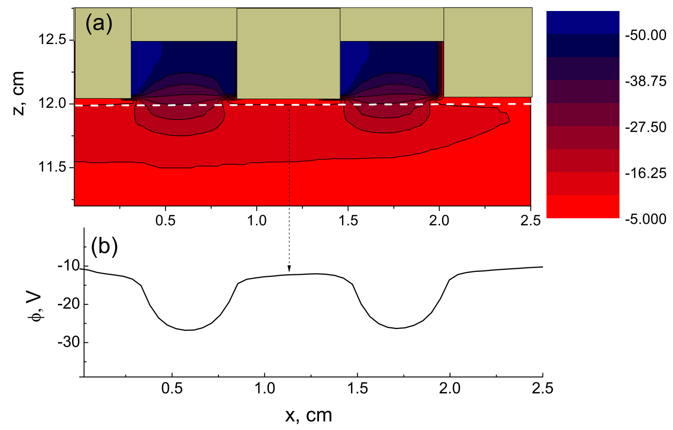

Figure 17. Calculated electric potential for $U = -190$ V. (b) shows the potential profile along the dashed line in (a).

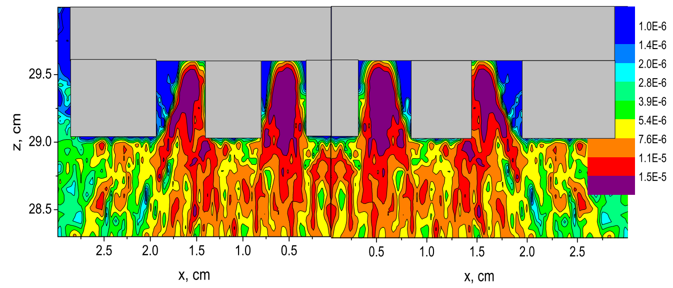

Figure 18. Spatial ion current density distribution (A/cm^2) near the surface with grooves of 5 mm wide and 5 mm depth for $U = -190$ V.

6. Non-uniformity of ion flux bombarding grooved emissive surface

The ion current to the emissive floating wall is much less than the electron current for a non-Debye type of sheath, nevertheless the energy of ions ε_i can be large enough for erosion of the wall. The ion motion is practically collisionless within the sheath for the gas pressure of 0.1 mTorr, and the ions gain the energy equal to the sheath potential drop. For the planar surface case, the energy is not sufficient for etching. Before the transition (see figure 12), when the sheath is developed, the energy of ions bombarding the emissive surface is less than 40 eV, and after the transition the ε_i becomes even 4–5 times smaller.

The flux of ions with much higher energy was revealed in simulations for the grooved emissive sample. As shown in figure 12, the critical voltage increases for the grooved surface and the ion energy can reach 60 eV for $U < U_{cr}$. Moreover, after the transition, the sheath potential drop decreases from (4–5)T_e to 1T_e only over the front segments of grooved surface, but not inside of grooves. The calculated potential distribution after the transition is shown in figure 17 for $U = -190$ V. It is seen that the collapsed sheath occurs only near the front segments of the sample. There the $\Delta\phi_s$ decreased from 48 V to 10 V at $U = U_{cr}$. Inside of the grooves the potential drop remains large accelerating the ions entering the trenches.

The component of the electric field parallel to the surface E_x can reach 100 V cm^{-1} and changes a sign at the orifice edges since the electric potential near the surface is modulated (see figure 17(b)). This E_x deflects the ion trajectories to orifices of grooves and electron ones in the opposite direction. The ions gain the energy crossing the potential drop inside of groove and the high-energy ion flux bombards the bottom of the grooves. The spatial distribution of ion current density j_i is shown in figure 18 for the potential distribution in figure 17. It is seen that the j_i is much higher at the bottom of grooves compared to the front surface one.

With increasing the cathode voltage from -190 V to -350 V the density of plasma increases, sheath near the emissive surface becomes thinner, but the focusing effect of modulated potential retains to be strong. In figure 19, the spatial potential and ion energy distributions near the surface with trenches are shown for $U = -350$ V.

The sheath potential drop near the front surface of grooves shown in figure 19(a) is essentially smaller compared to the $\Delta\phi_s$ inside of the grooves. The ion energy gradually increases from the orifice to the bottom of grooves (see figure 19(b)). The energy distributions of ions calculated on the front and bottom surfaces of grooves are shown in figure 20 for $U = -350$ V. The energy of ions approaching the front surface ranges from 20 to 50 eV, whereas the energy of ions on the bottom is (100–120) eV.

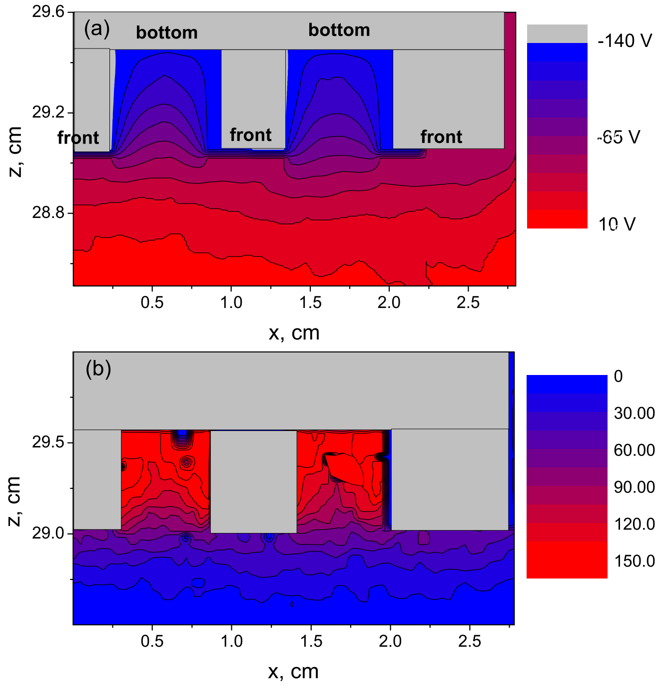

Figure 19. Spatial potential (a) and ion energy (b) distributions near the surface with trenches for $U = -350$ V.

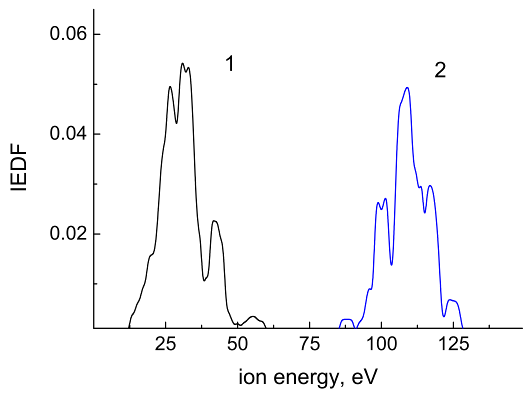

Figure 20. Energy distribution functions of ions approaching the front (1) and bottom (2) segments of trenches for $U = -350$ V.

7. Non-uniformity of ion flux induced a variation of SEE yield over the planar surface

The wall of the plasma device can be constructed from materials with the different SEE yields. In this case, modulation of surface potential and focusing the electron and ion fluxes are expected to increase a non-uniform etching. In this section, in numerical simulations, we study the sheath formation near the planar BN-sample with inserts of a model material instead of grooves discussed in section 6. The inserts are 5 mm wide, and their SEE coefficient is supposed to be four times less than for hBN for the entire electron energy range. This planar sample mimics the wall fabricated from different emissive materials.

In simulations, we found that the sheath near the segmented planar sample like in the case of a grooved one has a higher U_{cr} for the transition that the uniform planar sample. In figure 21, the spatial potential distribution next to the segmented planar sample is shown for the case of $U < U_{cr}$ and for the case of $U > U_{cr}$. The dark grey rectangles denote a model material with smaller SEE coefficient. As seen in figure 21(a), before the transition at $U = -190$ V the plasma-sample sheath is almost uniform. After the transition, the plasma-sample sheath becomes smaller next to segments with larger SEE yield and increases over the model-material with lower SEE yield. So we have found that the potential distribution is also modulated over the planar surface with inserts with different SEE yields.

In figure 22, the spatial distribution of the ion energy and the ion current density near the surface of the planar segmented sample are shown for $U = -330$ V. It is seen that the segments of material with lower SEE yield are exposed to the enhanced ion flux with high energy ions.

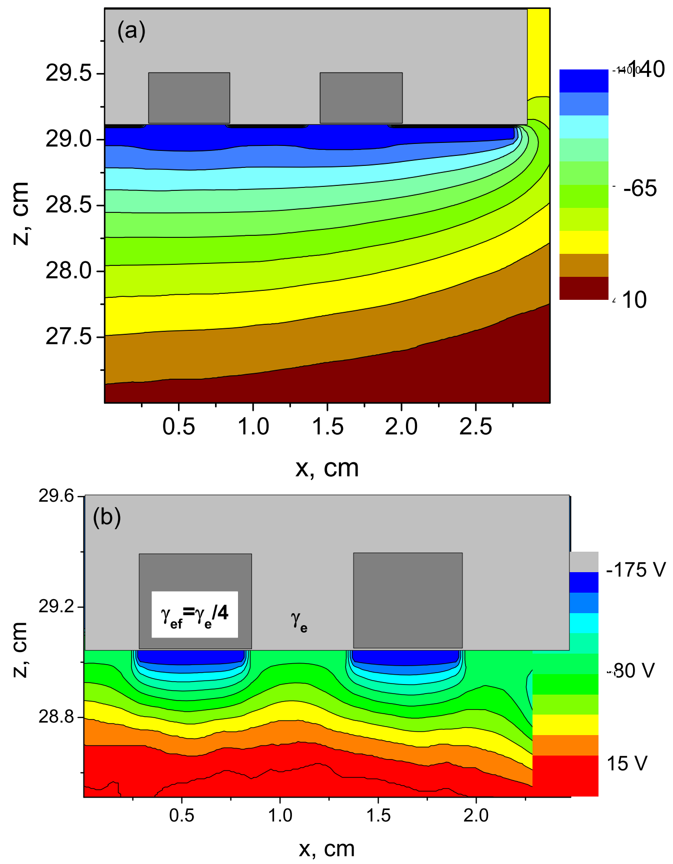

Figure 21. Spatial potential distribution for $U = -190$ V (a) and for $U = -330$ V (b) near the segmented planar sample.

In conclusion of this section, the sheath transition near the planar emissive segmented BN-sample which is electrically isolated have been studied in kinetic simulations. The planar sample has four inserts with SEE coefficient $\gamma = 0.25\ \gamma_{BN}$. We reveal that the modulation of the potential near the planar emissive segmented sample almost repeats the modulation observed for the grooved sample. An essentially higher energy ions bombard that part of the surface which has lower SEE. It is interesting to note, that as for grooved sample the transition from developed and collapsed types of sheath for planar segmented sample happens at essentially higher U_{cr} that for planar sample with uniform SEE.

8. Non-uniformity of electron and ion fluxes in discharge plasma controlled by external magnetic field

An external oblique magnetic field applied to low-pressure discharge plasma provokes the stratification of discharge plasma [17], which causes a modulation of ion and electron currents over the wall surface. To describe this effect of the rearrangement of discharge plasma in the electromagnetic field the system of equations including Boltzmann equations for the distribution functions for electrons and ions (1)–(2) and Poison equation for electric potential distribution (3) was solved with PIC MCC method. Here in our study, we make an accent on the non-uniformity of electron and ion fluxes near the wall of the plasma chamber at low gas pressure for different angles of magnetic fields and plasma parameters.

In simulations, the plasma is embedded in a cylindrical chamber with a radius of 4 cm and the height $H = 10$ cm. The calculation domain is shown in figure 23. The cathode made from metal material with a radius of 3 cm is placed 0.3 cm apart from the chamber bottom. The boundary conditions are the following: $\phi = -90$ V at the cathode, $\phi = 0$ at the wall of the chamber and $\delta\phi/\delta r = 0$ at $r = 0$.

The strength of external magnetic field B is assumed to be constant over the plasma volume. The magnetic field is axially symmetrical. The magnetic field angle α_B is taken in the following form to avoid the singularity at $r = 0$: $\alpha_B = 0$ at $r < r_1$, $\alpha_B = \alpha_{B0}$ at $r > r_2$, α_B is approximated by a quadratic spline function at $r_1 < r < r_2$, In simulations, we took $r_1 = 0.3$ cm and $r_2 = 0.6$ cm (see figure 23). For the case of $\alpha_B = 0$, the field B is parallel to the radial component of the electric field, E_r.

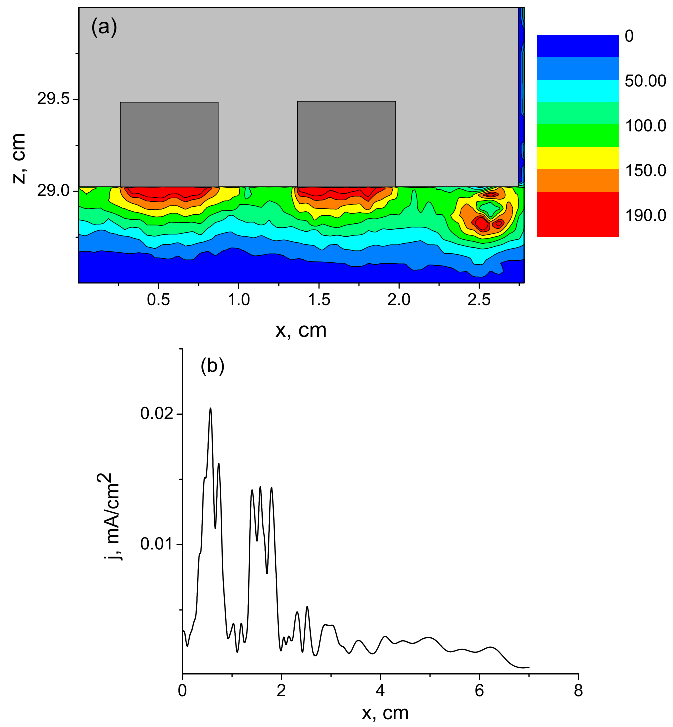

Figure 22. Spatial ion energy distribution (a) and profile of ion current density near the surface of the planar segmented sample for $U = -330$ V.

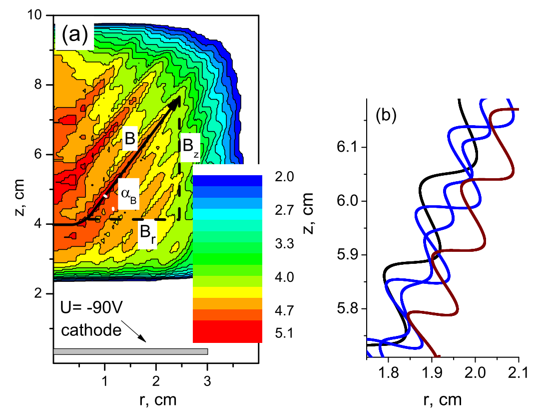

Figure 23. Spatial potential distribution in the cylindrical model plasma chamber (a). *B* denotes the magnetic field. Example of electron trajectories with different energies (b).

The ionization processes in the plasma are set by a) the external ionization with a given rate and b) the electron impact ionization calculated with PIC MCC method. The former is modeled as electron-ion pairs generation with the Maxwellian distributions over velocity with the mean electron temperature T_e and the ion temperature $T_i = 0.05$ eV. The latter is calculated with This external ionization can be provided by the radiation source or can mimic the plasma refilling from another source with Maxwellian plasma. The external ionization rate is assumed to be constant over the volume of the quasineutral plasma. The electron temperature T_e varies from 2.5 eV to 10 eV for different cases. The rate ν_i of the electron-ion pair generation is chosen to achieve the plasma density of $10^8 \mathrm{cm}^{-3}$ in the quasineutral part. For all cases the rate ν_i is equal to $2.5 \times 10^8 \mathrm{s}^{-1} \mathrm{cm}^{-3}$.

In simulations, the background gas density is $3.3 \times 10^{12} \mathrm{cm}^{-3}$ which refers to the gas pressure 10^{-4} Torr. The strength of the magnetic field *B* ranged from 25 G to 100 G and the angle $\alpha_B = 0 \div 77°$. For these plasma parameters the electron Larmor radius r_L is comparable to the Debye length λ_D, $r_L \approx \lambda_D$. The plasma frequency ω_p is about of the electron gyrofrequency Ω_e, $\omega_p \leqslant \Omega_e = 5 \times 10^8 \mathrm{s}^{-1} \div 5 \times 10^9 \mathrm{s}^{-1}$. In simulations, the electron time step Δt_e is $(2\text{–}5) \times 10^{-12}$ s, so $\Delta t_e \ll 1/\omega_p$, $1/\Omega_e$, $\Delta r/v_e$, $\Delta z/v_e$, where Δr, Δz are steps of calculation grid over axes r and z, and v_e is the maximum electron velocity. The 2D3V PIC MCC method [35, 36]

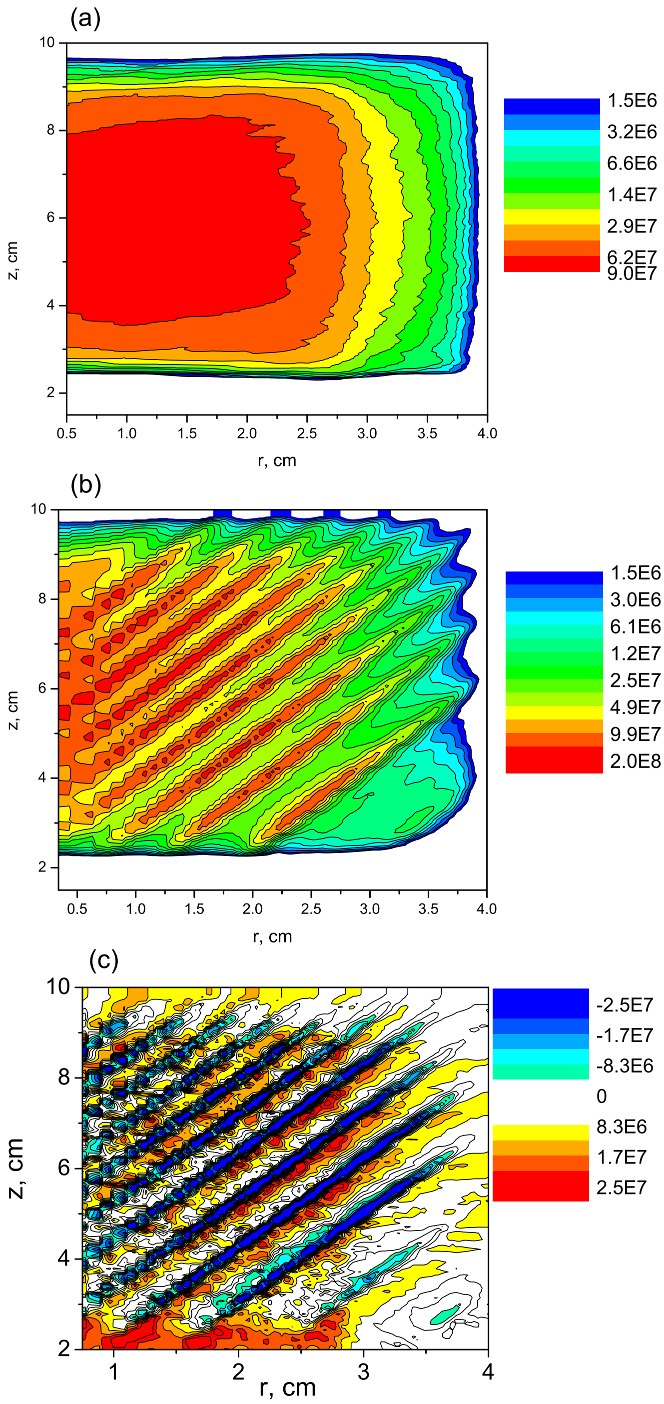

Figure 24. Distribution of electron density, n_e, cm^{-3} (linear scale), for $\alpha_B = 10°$ (a), 65°(b) and electric charge, $n_e - n_i$, cm^{-3} for 65° (c), B = 50 G, $T_e = 5$ eV.

used in simulations allows us to calculate the 3D trajectories of electron gyromotion with variable components of electron velocity. The 2D Poisson equation is solved at every electron time step. First, the electron and ion concentrations are calculated on the cylindrically symmetrical grid and then the potential and electric field distributions are calculated also for the cylindrically symmetrical grid.

In PIC MCC simulations, we revealed that a structure of discharge plasma is affected by the obliqueness of the external magnetic field (B-field). The rearrangement of plasma with α_B is shown in figures 23(a) and 24. An example of electron trajetories with different energy is shown in figure 23(b). The sheath with the potential drop $\Delta\phi$ of (93–97) V forms near the cathode. A weaker sheath with $\Delta\phi = (3–7)$ V screens plasma from the chamber wall. The sheaths can be seen in figure 24 as areas with the depleted electron density. The color palette in figure 23 ranges from 2 V to 5 V to show the potential steps over the quasineutral plasma appearing with increasing α_B. The electron density is almost uniform in the central part of the chamber for small α_B in

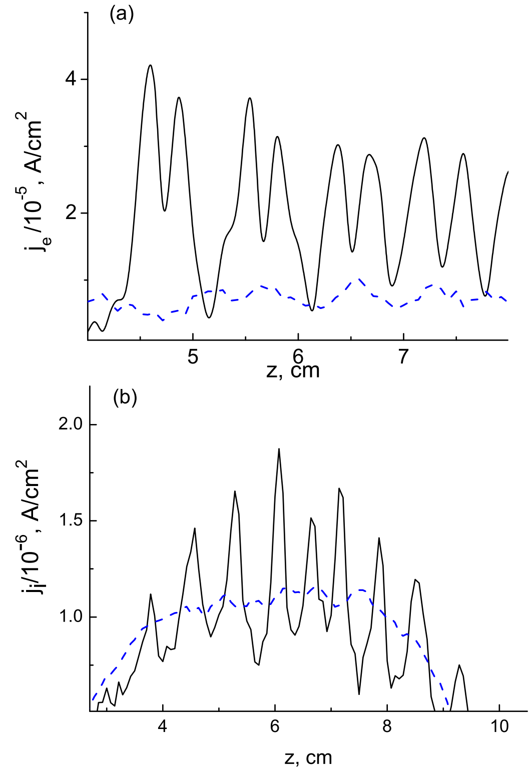

Figure 25. Distribution of electron current (a) and ion current (b) over z-axis near the side surface for $B = 50$ G, $\alpha_B = 65°$ and $\epsilon_e = 2.5$ eV.

figure 24(a), but for larger α_B the periodical plasma structure forms In figure 24(b), for $\alpha_B = 65°$, the electron density exhibits ridges oriented along the magnetic field vector. The ridges of electron and ion densities are shifted relatively each other across B-field (see figure 24(c)). The layers of negative and positive charges appear in quasineutral plasma. This structure is called as double-layers and characterized with the non-monotonic potential distribution shown in figure 23. The potential profile across the B-field have the potential drops of 0.2–0.5 V.

The double-layers form due to a distortion of local quasineutrality in the occurrence of the oblique magnetic field. It happens because after the ionization event a pair of electron and ion start Larmor gyromotion with very different radii. The electron is shifted from the ion in the direction normal to B-field, and a local charge appears. The uniform positive charge indicates the cathode sheath at $z < 2.7$ cm. The cathode sheath length is 2.3 cm.

The electron and ion current channels are associated with ridges of n_e and n_i. The currents are aligned with B-vector not only in the area of quasineutral plasma, but also within the sheath over the wall. In figure 25, the profiles of the radial component of the electron j_e and ion j_i currents near the wall are shown for two values of α_B. It is seen that both currents approaching the wall are affected by a variation of α_B. The j_e-profile over z taken at $r = 3$ cm is almost uniform for $\alpha_B = 10°$ and has peaks for $\alpha_B = 65°$. Each electron current peak is split with a scale of $2r_L$, where r_L is Larmor radius. The j_i-profile over z taken near the wall also exhibits peaks for larger α_B. An increase of the ion current and its peaked profile are typically observed in our simulations for larger α_B. This effect can lead to an additional local erosion of wall material.

In figure 26, the spatial distributions of plasma parameters near the side wall are shown for $B = 100$ G. The radial component of ion current density near the wall is shown in figure 26(a)). The white lines denote the approximate boundary between the bulk plasma and wall sheath. In the quasineutral plasma, the ion current is oriented along n_i-ridges, but within the wall sheath, the j_i turns to the direction normal to the wall due to a stronger electric field. All plasma parameters, the ion density, electric potential and charge ($n_e - n_i$) shown in figures 26(b)–(d) constitute the periodical structure induced by the inclined external magnetic field. This periodic structure retains within the wall sheath that leads to the nonuniform wall bombardment by electron and ion fluxes.

With increasing T_e and decreasing B, the distance between plasma ridges (the period length) becomes larger. The period length of the multi-step double-layer structure is shown in figure 27 as a function of r_L for $\alpha_D = 65°$. It is seen that the inter-peak distance increases with Larmor radius.

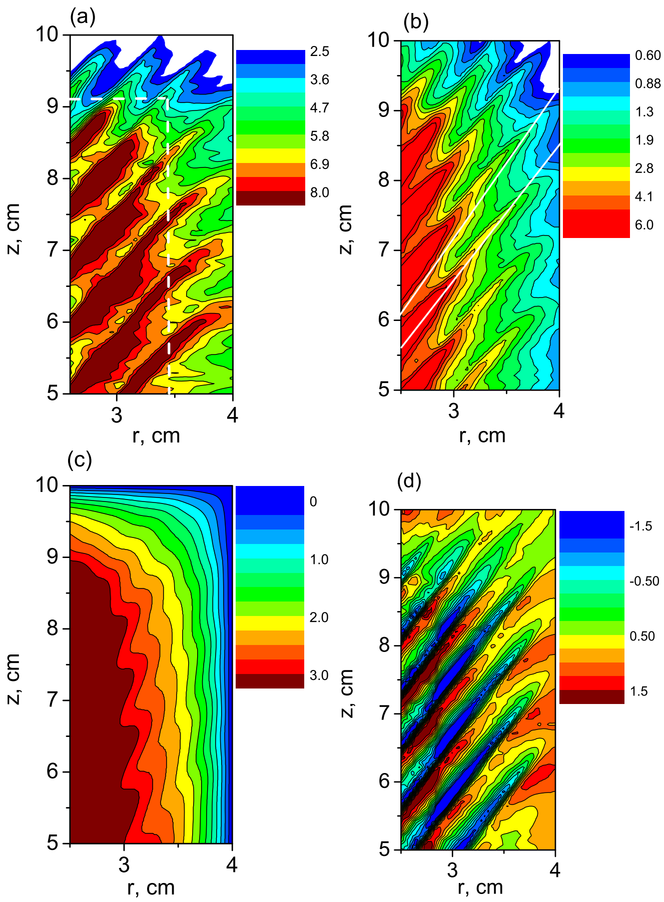

Figure 26. Spatial distribution of radial component of ion current density (a), ion concentration (b), electric potential (c) and charge density (d) for B = 100 G, $\alpha_B = 65°$ and $\epsilon_e = 5$ eV.

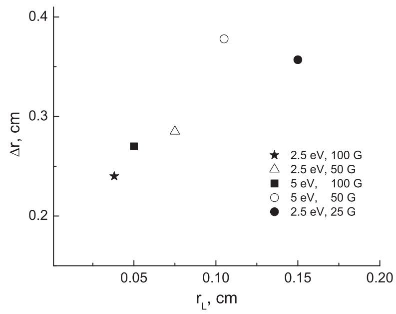

Figure 27. Period length of periodical structure from r_L for different T_e and B, $\alpha_B = 65°$. Figure 8 in [42].

In the limit of large $r_L \sim T_e^{0.5}/\mathrm{B}$ and small n_e the plasma becomes smoother since the Larmor radius and inter-peaks distance are comparable. With decreasing $T_e^{0.5}/\mathrm{B}$ and increasing n_e the plasma forms more and more sharp peaks. We resolve 19 peaks for the case of $\alpha_B = 65°$ and $r_L = 0.07$ cm ($T_e = 2.5$ eV and B = 100 G).

For the close value of r_L, but different T_e and B, the plasma structure looks similar. The difference is due to the variation of λ_D for different cases since the plasma density depends on the potential drop near the wall, which in turn is a function of the electron energy.

The modulation of electron current near the wall sample in the plasma under similar conditions (B = 25–100 G, $T_e = 2$ eV, $n_e = 5\times10^6\mathrm{cm}^{-3}$–$5 \times 10^8\mathrm{cm}^{-3}$) in crossed electromagnetic fields was measured in [45]. In this experiment, the sample was rotated, changing the angle relatively magnetic field vector. The measurements were done perpendicular to the sample surface at distance 6, 8, and 10 mm. From the

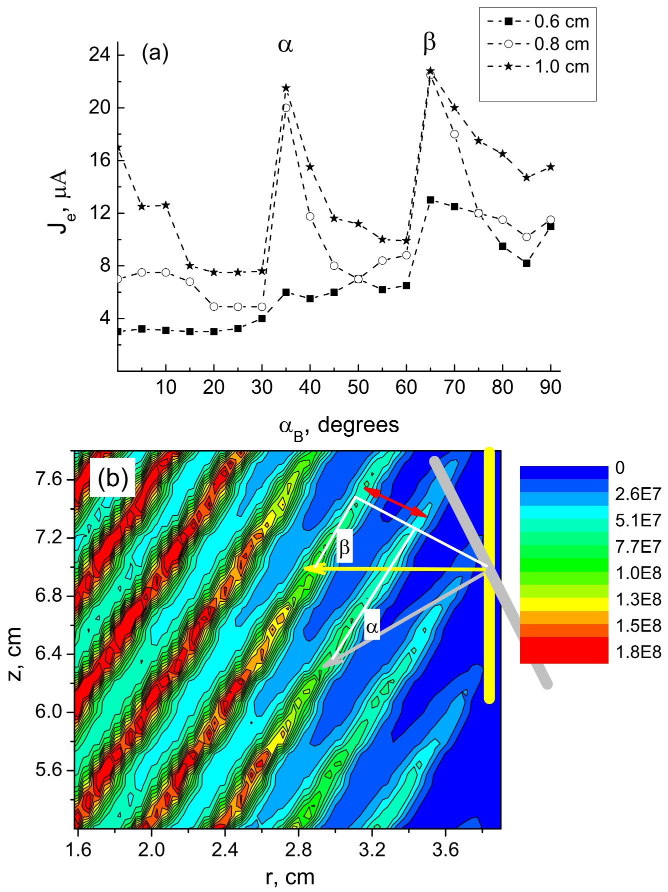

Figure 28. (a) Measured electron current as a function of α_B for 0.6 cm, 0.8 cm and 1 cm from the wall and (b) electron den- sity distribution for B = 100 G and Te = 2 eV. Angles $\alpha_B = 35°$ and $\alpha_B = 65°$ show the angles between magnetic field vector and normal to the wall. Yellow and white arrows show the direction of measurements from the wall (thick yellow and white lines).

comparison of experimental and theoretical data in figures 28(a) and (b), it is clear that when the plate is rotating, a tip of the probe crosses the maxima and minima of the electron density. Note that the peak of electron density coincides with current channels. The inter-peak distance calculated from experimental data shown in figure 28(a) is 0.35 cm. Since our discharge geometry is not the same as the one in the experiment we did not give the direct comparison of simulation and experimental results. However, the phenomena of multiple layer formation observed in our simulations and in the experiment [18] in discharge plasma induced by the oblique magnetic field are very similar.

9. Conclusion

In the experiment and kinetic simulations, we considered the origins of appearance of a spatial non-uniform distribution of ion and electron currents to the wall of plasma chamber at low gas pressure. It was shown that the non-planar plasma sheath forms near the emissive surface with the Debye-size grooves. This non-planar sheath redistributes the ion and electron fluxes over the surface. The non-uniformity of plasma currents to the wall becomes even more pronounced after the plasma sheath transition and the ion current is gathered to the orifices of the grooves. The similar phenomenon was found for the segmented surface made from the material with different coefficients of the secondary electron emission. The spatial alteration of ion fluxes was registered and the higher ion current to the fragments with the smaller SEE.

The periodical structure with the ridges of ion and electron densities is induced by applying the oblique magnetic field to the dc discharge plasma. The ridges of electron and ion densities are shifted with respect to each other, and the double-layer structure appears across B-field and along the potential rise. The ion and electron currents are aligned with B-vector not only in the area of the quasineutral plasma but also within the sheath over the wall providing non-uniform stress on the wall.

Acknowledgments

The authors gratefully acknowledge FA9550-11-1-0160, Program Manager Mitat Birkan for support of this research. One of the authors, IS, was partly supported by RSF 17-19-01375.

ORCID iDs

I V Schweigert https://orcid.org/0000-0002-2364-1228

References

[1] Arkhipov B A, Gnizdor R Y, Maslennikov N A and Morozov A I 1992 *Sov. J. Plasma Phys.* **18** 641
[2] Keidar M, Boyd I D and Beilis I I 2001 *Phys. Plasmas* **8** 5315
[3] De Grys K, Mathers A, Welander B and Khayms V 2010 *XLVI AIAA/ASME/SAE/ASEE Joint Propulsion Conf. and Exhibit (AIAA)* 2010–6698
[4] Gascon N, Dudeck M and Barral S 2003 *Phys. Plasmas* **10** 4123
[5] Barral S, Makowski K, Peradzynski Z, Gascon N and Dudeck M 2003 *Phys. Plasmas* **10** 4137
[6] Hofer R R, Mikellides I G, Katz I and Goebel D M 2007 *XXX International Electric Propulsion Conf., IEPC-2007-267 17*
[7] Burton T, Schinder A M, Capuano G, Rimoli J J, Walker M L and Thompson G B J 2014 *Propulsion and Power* **30** 690
[8] Langendorf S and Walker M 2015 *Phys. Plasmas* **22** 033515
[9] Raitses Y, Staack D, Dunaevsky A and Fisch N 2006 *J. Appl. Phys.* **99** 361031
[10] Hobbs G D and Wesson J A 1967 *Plasma Phys.* **9** 85
[11] Sydorenko D, Kaganovich I, Raitses Y and Smolyakov A 2009 *Phys Rev Lett.* **103** 145004
[12] Campanell M D, Khrabrov A V and Kaganovich I D 2012 *Phys. Rev. Lett.* **108** 255001
[13] Morozov A I and Savel'ev V V 2007 *Plazma Phys. Reports* **33** 20
[14] Keidar M, Boyd I D and Beilis I I 2001 *Phys. Plasmas* **8** 5315
[15] Sheehan J P, Hershkowitz N, Kaganovich I D, Wang H, Raitses Y, Barnat E V, Weatherford B R and Sydorenko D 2013 *Phys. Rev. Lett.* **111** 075002
[16] Schweigert I V, Langendorf S J, Walker M L R and Keidar M 2015 *Plasma Sources Sci. Technol.* **24** 025012 (9pp)
[17] Schweigert I, Burton T S, Thompson G B, Langendorf S, Walker4 M L R and Keidar M 2018 *Plasma Sources Sci. Technol.* **27** 045004
[18] Velikhov E P and Dykhne A M 1963 *VI Conf. Internationale sure les Phenomenes d'Ionisation sur les Gaz (Paris)* 4, 511
[19] Kerrebrock J L 1964 *AIAA Jnl 2* **I072** 0964
[20] Miedzik J, Barral S and Danilko D 2015 *Phys. Plasmas* **22** 043511
[21] Xu K G, Dao H and Walker M L R 2012 *Phys. Plasmas* **19** 103502
[22] Intrator T, Menard J and Hershkowitz N 1993 *Phys. Fluids* B **5** 806
[23] Borovsky J E and Joyce G 1983 *J. Plasma Phys.* **29** 45
[24] Ergun R E *et al* 2001 *Phys. Rev. Lett.* **87** 045003
[25] Ergun R E *et al* 2009 *Phys. Rev. Lett.* **102** 155002
[26] Mozer F *et al* 2013 *Phys. Rev. Lett.* **111** 235002
[27] Malaspina D M *et al* 2014 *Geophys. Res. Lett.* **41** 5693
[28] Malaspina D M *et al* 2015 *J. Geophys. Res.: Space Phys.* **120** 4246
[29] Limpaecher R and MacKenzie K R 1973 *Rev. Sci. Instrum.* **44** 726
[30] Oksuz L and Hershkowitz N 2002 *Phys. Rev. Lett.* **89** 145001
[31] Sheehan J and Hershkowitz N 2011 *Plasma Sources Sci. Technol.* **20** 063001
[32] Hershkowitz N, DeKock J R, Coakley P and Cartier S L 1980 *Rev. Sci. Instrum.* **51** 64
[33] Knappmiller S, Robertson S and Sternovsky Z 2006 *Phys. Rev.* E **73** 066402
[34] Hagstrum H D 1954 *Phys. Rev.* **96** 325
[35] Birdsall C K 1991 *IEEE Trans. Plasma Sci.* **19** 66
[36] Birdsall C K and Langdon A B 1991 *Plasma Physics via Computer Simulations* (Bristol: IOP)
[37] Ivanov V V, Popov A M and Rakhimova T V 1995 *Sov. Plasma Phys.* **21** 548
[38] Lagushenko R and Maya J 1984 *J. Appl. Phys.* **59** 3293
[39] Tondu T, Belhaj M and Inguimbert V 2011 *J. Appl. Phys.* **110** 093301
[40] Babovsky H and Ilner R 1989 *SIAM J. Num. Anal.* **26** 45
[41] Intrator T, Cho M H, Wang E Y, Hershkowitz N, Diebold D and DeKock J 1988 *J. Appl. Phys.* **64** 2927
[42] Schweigert I V and Keidar M 2017 *Plasma Sources Sci. Technol.* **26** 064001
[43] Bugeat J P and Koppel C 1995 *XXIII Int. Conf. on Electric Propulsion, IEPC* 95–35
[44] Schmidt N, Schulze J, Schungel E and Czarnetzki U 2013 *J. Physics D: Appl. Phys.* **46** 505202
[45] Lukas J N 2016 *PhD Thesis* George Washington University